FEBS Letters 581 (2007) 5454–5458

Structural basis of mercury- and zinc-conjugated complexes as SARS-CoV 3C-like protease inhibitors

Cheng-Chung Lee[a,b,c], Chih-Jung Kuo[b,e], Min-Feng Hsu[b,c], Po-Huang Liang[c,d,e,g], Jim-Min Fang[d,f], Jiun-Jie Shie[d], Andrew H.-J. Wang[a,b,c,d,e,g,*]

[a] *Structural Biology Program, Institute of Biochemistry and Molecular Biology, National Yang-Ming University, Taipei 11221, Taiwan*
[b] *Institute of Biological Chemistry, Academia Sinica, Taipei 11529, Taiwan*
[c] *National Core Facility of High-Throughput Protein Crystallography, Academia Sinica, Taipei 11529, Taiwan*
[d] *The Genomics Research Center, Academia Sinica, Taipei 11529, Taiwan*
[e] *Taiwan International Graduate Program, Academia Sinica, Taipei 11529, Taiwan*
[f] *Department of Chemistry, National Taiwan University, Taipei 10617, Taiwan*
[g] *Institute of Biochemical Sciences, National Taiwan University, Taipei 10617, Taiwan*

Received 24 September 2007; revised 25 October 2007; accepted 25 October 2007

Available online 5 November 2007

Edited by Richard Cogdell

Abstract **Five active metal-conjugated inhibitors (PMA, TDT, EPDTC, JMF1586 and JMF1600) bound with the 3C-like protease of severe acute respiratory syndrome (SARS)-associated coronavirus were analyzed crystallographically. The complex structures reveal two major inhibition modes: Hg^{2+}-PMA is coordinated to C^{44}, M^{49} and Y^{54} with a square planar geometry at the S3 pocket, whereas each Zn^{2+} of the four zinc-inhibitors is tetrahedrally coordinated to the H^{41}–C^{145} catalytic dyad. For anti-SARS drug design, this Zn^{2+}-centered coordination pattern would serve as a starting platform for inhibitor optimization.**

Keywords: SARS; Metal ion; Protease inhibitor

1. Introduction

Severe acute respiratory syndrome-associated coronavirus (SARS-CoV) is an enveloped, positive-stranded RNA virus belonging to *Coronaviridae*, which caused the SARS outbreak in 2003. Other members of human coronaviruses include HCoV-229E, HCoV-OC43, HCoV-HKU1 and HCoV-NL63. For SARS-CoV, its 3C-like protease ($3CL^{pro}$) functions in the maturation of viral proteins, thus representing an ideal target for therapeutic intervention [1]. Its crystal structure [2,3] has been determined to assist the design of inhibitors [4,5].

We previously found that some metal ions (e.g., Cu^{2+}, Hg^{2+}, Zn^{2+}) and their metal-conjugated compounds [phenylmecuric acetate (PMA), toluene-3,4-dithiolato zinc (TDT), and *N*-ethyl-*N*-phenyldithiocarbamic acid zinc (EPDTC)] showed inhibitory potency in the low or sub-μM range against SARS-CoV $3CL^{pro}$ [6]. Hg^{2+} or Zn^{2+} were known to inhibit several viral proteases such as $3CL^{pro}$ of norovirus, papain-like protease (PLP2) of SARS-CoV, human cytomegalovirus (hCMV) protease and hepatitis C virus (HCV) NS3 protease [7–11]. Here, to elucidate the metal-inhibitor binding mode and to pursue better inhibitors, we extended our work to two zinc-based inhibitors bis(L-aspartato-*N*,*O*) zinc(II) ethanate (designated as JMF1586) and (nitrilotriacetato-*N*,*O*) zinc(II) acetate (designated as JMF1600) and obtained the crystal structures of SARS $3CL^{pro}$ complexed with PMA, TDT, EPDTC, JMF1586 and JMF1600 to delineate the inhibition modes.

2. Materials and methods

2.1. Inhibitors and inhibition assay

JMF1856 and JMF1600 were prepared according to the following procedure. Et_3N (10 mmol) was added to a mixture of L-aspartic acid (10 mmol) or nitrilotriacetic acid (5 mmol) in ethanol. The reaction mixture was stirred at room temperature, prior to the addition of zinc acetate dihydrate (5 mmol). The white precipitate was collected by filtration, and washed with ethanol and acetone to yield the desired zinc complex. These complexes were characterized by nuclear magnetic resonance (NMR) spectra and electrospray ionization mass spectrometry (ESI-MS). Their molecular formula are shown in Scheme 1.

The fluorimetric assay was utilized to identify inhibitors of SARS-CoV $3CL^{pro}$ and determine their inhibition constants [12]. The K_i values of PMA, EPDTC, and TDT against $3CL^{pro}$ have been reported [6], and those of JMF1600 and JMF1586 was 0.32 μM and 0.05 μM, respectively.

2.2. Crystallization, data collection and structure determination

The purified SARS-CoV $3CL^{pro}$ was prepared as described previously [2]. All inhibitors were dissolved in DMSO for crystallization. Using the sitting-drop vapor diffusion method, enzyme solution was mixed with inhibitor solutions by a molar ratio of 1:5 for 20 min before combining with equal amounts of reservoir. The $3CL^{pro}$-EPDTC crystals were obtained using a reservoir of 10% PEG 6000, 14% DMSO, 2 mM DTT, 0.1 M MES at pH 6.5. The other complex crystals were obtained using 15% PEG 6000, 4–14% DMSO, 0.1 mM DTT, and 0.1 M MES at pH 6.5. The crystals were flash-frozen to 100 K with 20–25% ethylene glycol (vol/vol) as a cryo-protectant. The $3CL^{pro}$-JMF1586 data were collected at the wavelength of 1.000 Å using Taiwan beam line BL12B2 in SPring8 (Japan). Data sets for the other four crystals were collected using the MSC MicroMax 002 equipped with an R-AXIS IV^{++} image-plate detector. Diffraction data were processed and scaled using the program HKL2000 [13].

*Corresponding author. Address: Institute of Biological Chemistry, Academia Sinica, Taipei 11529, Taiwan. Fax: +886 2 2788 2043.
E-mail address: ahjwang@gate.sinica.edu.tw (A.H.-J. Wang).

Abbreviations: BABIM, bis(5-amidino-2-benzimidazolyl) methane; EPDTC, *N*-ethyl-*N*-phenyldithiocarbamic acid zinc; ESI-MS, electrospray ionization mass spectrometry; JMF1586, bis(L-aspartato-*N*,*O*) zinc(II) ethanate; JMF1600, (nitrilotriacetato-*N*,*O*) zinc(II) acetate; NMR, nuclear magnetic resonance; PMA, phenylmercuric acetate; TDT, toluene-3,4-dithiolato zinc

0014-5793/$32.00
doi:10.1016/j.febslet.2007.10.048

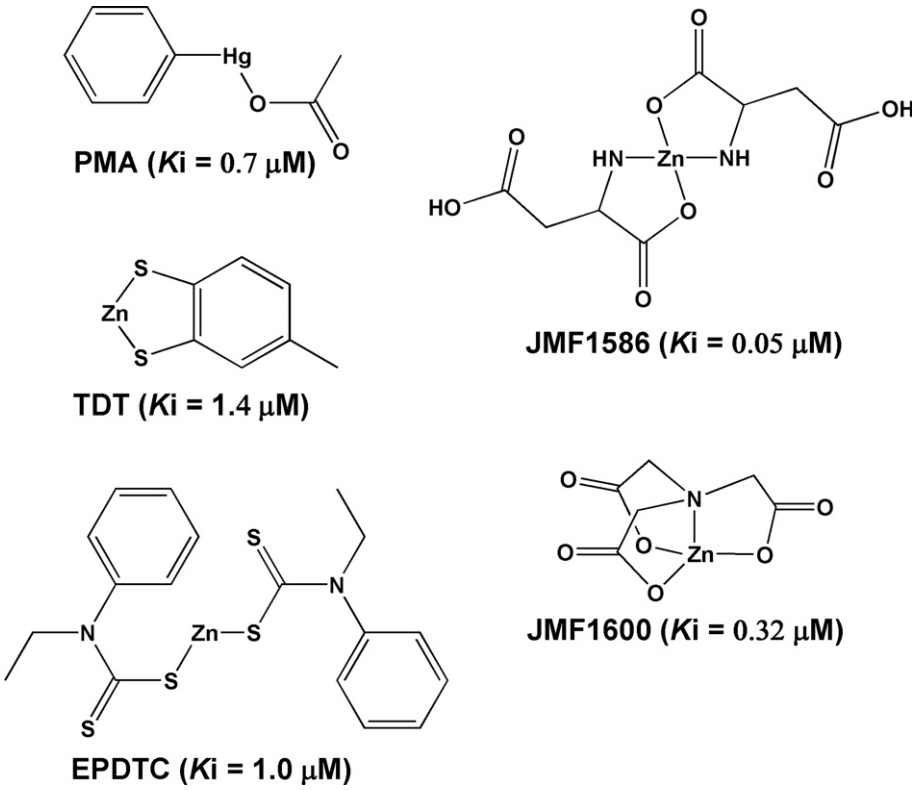

Scheme 1. Chemical structures and inhibition parameters of inhibitors. PMA is a mercury-conjugated compound, whereas TDT, EPDTC, JMF1586 and JMF1600 are zinc-conjugates. The respective inhibition constants (K_i) for SARS-CoV 3CL^{pro} are also indicated.

All crystal structures were determined by molecular replacement method using the program AMoRe [14], and using Protein Data Bank (PDB) code 1Z1J [2] as the search model. The Crystallography and NMR System (CNS) program [15] was used for structure refinement. All manual modifications of the models were performed using the program XtalView [16]. The difference Fourier map ($F_o - F_c$) was used to locate the inhibitors and solvent molecules. Data collection and final model statistics are shown in Table S1. The atomic coordinates and structure factors of 3CL^{pro}-EPDTC, 3CL^{pro}-JMF1600, 3CL^{pro}-JMF1586, 3CL^{pro}-PMA and 3CL^{pro}-TDT have been deposited in the Protein Data Bank codes 2Z9J, 2Z9K, 2Z9L, 2Z9G and 2Z94, respectively.

3. Results

3.1. Overall structures

SARS-CoV 3CL^{pro} is a homodimer with three domains in each monomer. Its active site comprises the His^{41}-Cys^{145} catalytic dyad located at the cleft between domains I and II, and the third domain contributes to the dimerization of protease [2,3] (Fig. 1A). Here, five complex structures were determined. Diffraction data of the 3CL^{pro}-JMF1586 crystal were processed for anomalous signal and exploited to locate the zinc atom sites by calculating anomalous difference Fourier maps. Two major Zn^{2+} peaks were located in the active site of each protein molecule in the asymmetric unit. In the 3CL^{pro}-EPDTC, 3CL^{pro}-JMF1600, 3CL^{pro}-JMF1586 complex structures, four DMSO molecules in each dimer derived from the crystallization condition were found. Two were located on the enzyme surface surrounded by the side chains of R^{298}, M^{6}, and F^{8} of each subunit. The second pair of DMSO molecules was bound in the S1 pocket, which consists of the side chains of H^{163} and F^{140} and the main-chains of M^{165}, E^{166} and H^{172}. The oxygen atom of DMSO is hydrogen bonded to the imidazole side chain of H^{163} with a mean distance of 2.55 Å (Fig. 1A,B).

3.2. Binding mode of PMA, TDT and EPDTC

In the 3CL^{pro}-PMA complex structure, the phenyl-bound mercury is bound to the sulfur atom of residue C^{44} with the bond distance of 2.5 Å, and the phenolic oxygen atom of Y^{54}and sulfur atom of M^{49} serve as the other two ligands to form a square planar geometry with Hg–O and Hg–S bond lengths of 2.6 Å and 3.5 Å, respectively (Fig. 1C). The observed electron density of the inhibitor is well defined for mercury and the phenyl group, but the acetate group of PMA was dissociated and replaced by protein ligands. Furthermore, the phenyl group of PMA occupying the S3 pocket contacts the side chain of H^{41}, causing its imidazole ring to rotate to form a hydrogen bond (3.0 Å) with the backbone carbonyl oxygen of H^{164} (Fig. 1D). Comparison of 3CL^{pro}-PMA with the native-3CL^{pro} (PDB code 1Z1I) [2] structure reveals a significant conformational change of residues 43–51, indicating its flexibility for PMA entry to and binding at the S3 pocket.

TDT is bound to the catalytic dyad residues H^{41} and C^{145} acting to inhibit the enzyme's activity (Fig. 2A). The zinc atom of TDT is coordinated to the side chain nitrogen atom of H^{41} and the sulfur atom of C^{145} with a distorted tetrahedral geometry despite a rigid S–Zn–S bond angle of 93.3° (Fig. 2E). The toluene group of TDT has no interaction with the protein. The inhibition mode of EPDTC is the same as that of TDT regarding the zinc atom coordination to two sulfur atoms and two

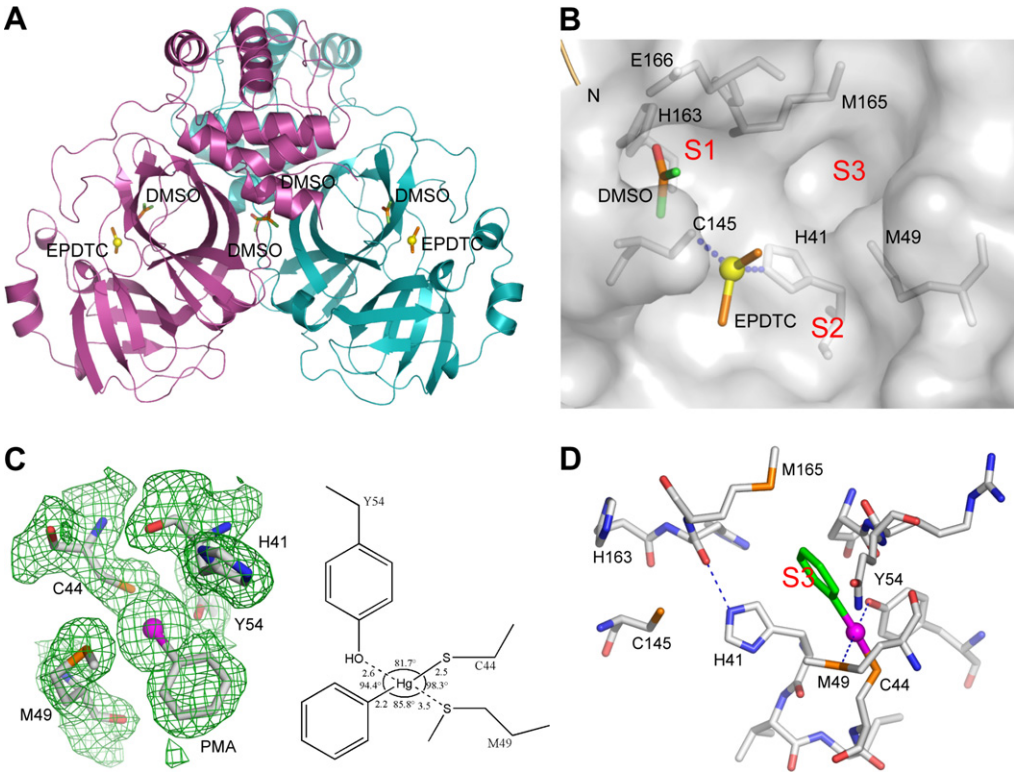

Fig. 1. Crystal structures of inhibited3CL^{pro}. (A, B) The overall three-dimensional structure and active site of 3CL^{pro} with the bound EPDTC and DMSO. The substrate binding subsites are designated as S1, S2, and S3. (C, D) The active site of 3CL^{pro} with the bound PMA. (C) The $2F_o - F_c$ electron density maps (1.0 σ level) and schematic representation of PMA coordination geometry with the bond lengths and bond angles indicated. (D) The phenyl-bound mercury is covalently attached to C^{44} and coordinated to Y^{54} and M^{49}. The oxygen atoms are red, nitrogen blue, sulfur orange, and carbon on protein gray. The inhibitor carbon atoms are green, and mercury is magenta sphere.

side chains of H^{41} and C^{145} (Fig. 2B). Nonetheless, the local metal center geometry of EPDTC, unlike that of TDT, is that the zinc ion binds to H^{41} and C^{145} in a more typical zinc tetrahedral geometry with the S–Zn–S bond angle of 107.2° (Fig. 2F). Moreover, the electron density map of the zinc atom and two sulfur atoms of EPDTC can be clearly seen in each subunit, yet the bulky substituent groups are absent (Fig. S1). The lack of electron density might suggest that the substituents are disordered. We have performed a computer modeling study to address the question whether the bulky substituents impede the binding of the complex. Fig. S2 shows that the entire EPDTC could be accommodated in the active site pocket, with sufficient room for the bulky side groups to rotate about. Therefore conformational disorder of side chains remains a likely possibility.

3.3. Binding modes of JMF1586 and JMF1600 and inhibition activity

JMF1600 and JMF1586 showed smaller K_i value (0.32 μM and 0.05 μM, respectively) for inhibiting SARS-3CL^{pro} than that of Zn^{2+} (1.1 μM) [6] by 3- and 20-fold, respectively (Scheme 1), with JMF1586 exhibiting the highest inhibition activity. In the 3CL^{pro}-JMF1586 complex, the zinc-centered tetrahedral coordination is formed by H^{41}, C^{145} and two nitrogen atoms. On the other hand, H^{41}, C^{145}, one nitrogen atom and a water molecule are responsible for the Zn coordination in the 3CL^{pro}-JMF1600 complex (Fig. 2C,D). Scheme 1 shows that the zinc atom is chelated by two nitrogen and two oxygen atoms for JMF1586, and by one nitrogen and three oxygen atoms for JMF1600. The Zn–N bond is stronger than the Zn–O bond, consistent with the lower K_i value for JMF1586. Both structures indicate that the metal–oxygen bond of JMF1586 and JMF1600 must break prior to being substituted by H^{41} and C^{145} in the formation of the zinc-centered complex. Like the case above, the electron densities of the zinc ions and nitrogen atoms of JMF1586 and JMF1600 were visible, but not those for the substituent groups (Fig. S1).

4. Discussion

In this study, five crystal structures allow us to identify ligand binding regions of metal-conjugated compounds as inhibitors of SARS-CoV 3CL^{pro}. The 3CL^{pro}-PMA structure reveals that a phenyl-bound mercury occupying the S3 pocket is responsible for inhibiting the enzymatic activity. One SARS-CoV 3CL^{pro} molecule contains 12 free cysteine-SH residues, in which only C^{44}, but not the active site C^{145}, provides a specific coordination environment for the phenyl-bound mercury. Inorganic Hg ion is known to cause toxic effects, since the affinity of Hg(II) ion to thiol group in proteins lead to non-specific inhibition of cellular enzymes [17]. Therefore, structural studies of the specific interaction between mercury-conjugated compounds and the thiol groups of cysteine-containing enzyme may be valuable for the future development of specific inhibitors.

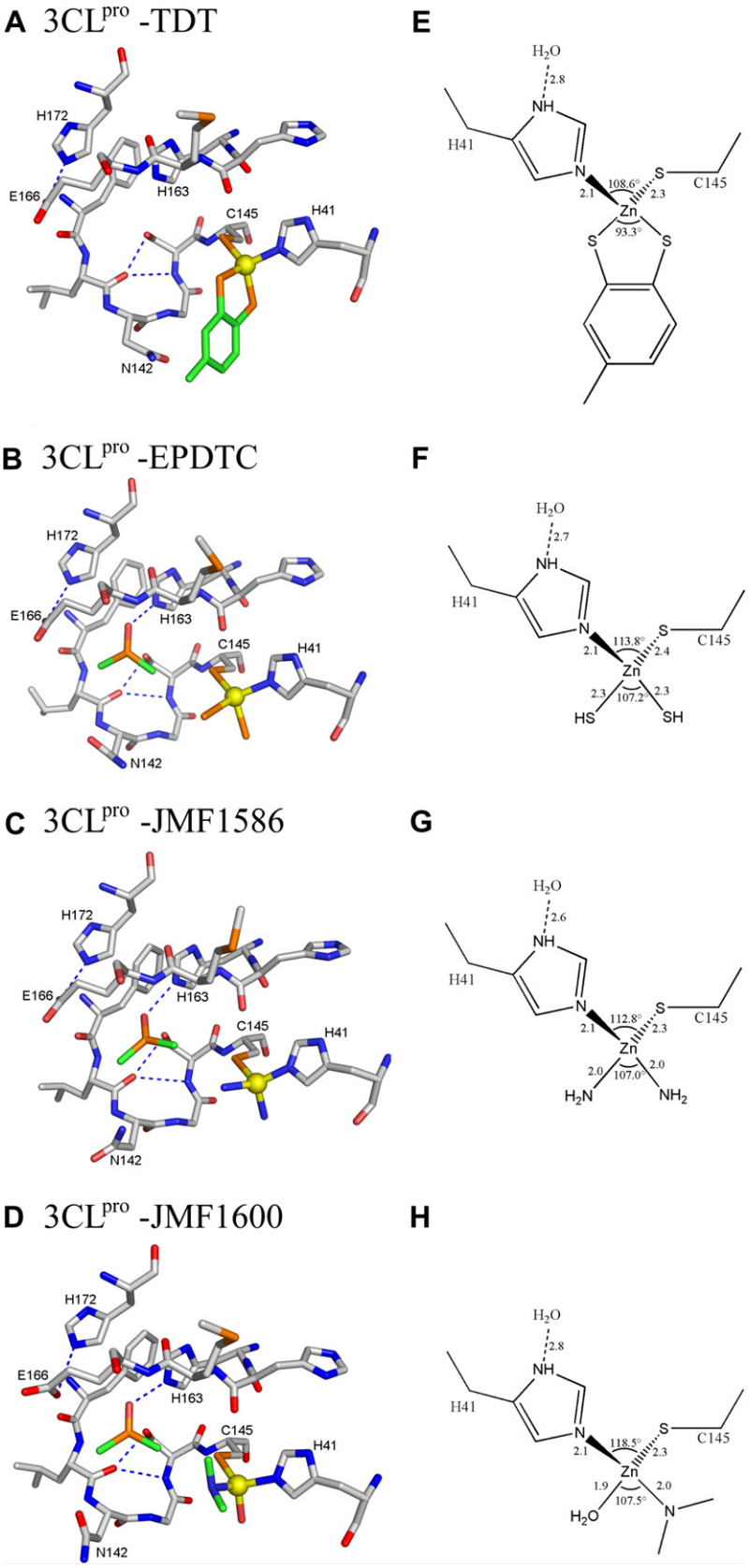

Fig. 2. Zinc-conjugated compounds bound to SARS-CoV $3CL^{pro}$. (A–D) The zinc inhibitors are coordinated to the catalytic dyad with the zinc ion surrounded by a tetrahedral or distorted tetrahedral arrangement of ligands. A DMSO molecule located at the S1 pocket was observed in the latter three crystals B, C and D, colored as in Fig. 1D. In all complexes, DMSO and inhibitors carbon atoms are green. The zinc ions are depicted as a yellow sphere. (E–H) Schematic representation of zinc-centered geometry in active sites. The zinc centered coordination is $N_{His}S_{Cys}S2$ for $3CL^{pro}$-TDT and $3CL^{pro}$-EPDTC, $N_{His}S_{Cys}N2$ for $3CL^{pro}$-JMF1586, and $N_{His}S_{Cys}ON$ for $3CL^{pro}$-JMF1600. The bond lengths and bond angles are also indicated.

Regarding the structures of the zinc-centered complexes, the zinc ion plays a key role in targeting the catalytic residues, via binding to the H^{41}–C^{145} catalytic dyad to yield a zinc-central tetrahedral geometry. This type of inhibition is similar to the zinc-mediated serine protease inhibitor keto-BABIM-Zn^{2+} for trypsin in that a zinc ion is coordinated to two chelating nitrogen atoms of bis(5-amidino-2-benzimidazolyl) methane (BABIM) and two catalytic residues (Ser-His) of trypsin in a tetrahedral geometry [18]. However, this zinc-centered inhibition mode has never been described before for cysteine protease. The safety of zinc-containing compounds for human use is indicated by the fact that zinc acetate and zinc sulfate are added as a supplement to the drug for the treatment of Wilson's disease and Behcet's disease, respectively [19,20]. The possibility of zinc complexes incorporated into cells through the cell membrane is also demonstrated by the studies on type 2 diabetic treatment [21]. Here, our results show that the zinc-centered coordination pattern would serve as a starting platform for inhibitor optimization and the development of potential drug for SARS therapies. Since 3C and 3CL proteases with the Cys-His catalytic residues have been found in several human viruses such as the family of *Coronaviridae*, and *Arteriviridae* [22,23], these proteases can be targets for the zinc derivatized inhibitors.

Acknowledgements: We acknowledge the National Synchrotron Radiation Research Center of Taiwan, SPring-8 of Japan for beam time allocation. We thank Dr. T.-P. Ko for critical review of the manuscript. This work was supported by grants from Academia Sinica and the National Science Council, Taiwan NSC-93-3112-B-001-011-Y to A.H.-J. Wang for the National Core Facility of High-Throughput Protein Crystallography at Academia Sinica, Taiwan.

Appendix A. Supplementary material

Supplementary data associated with this article can be found, in the online version, at doi:10.1016/j.febslet.2007.10.048.

References

[1] Weiss, S.R. and Navas-Martin, S. (2005) Coronavirus pathogenesis and the emerging pathogen severe acute respiratory syndrome coronavirus. Microbiol. Mol. Biol. Rev. 69, 635–664.
[2] Hsu, M.F. et al. (2005) Mechanism of the maturation process of SARS-CoV 3CL protease. J. Biol. Chem. 280, 31257–31266.
[3] Yang, H. et al. (2003) The crystal structures of severe acute respiratory syndrome virus main protease and its complex with an inhibitor. Proc. Natl. Acad. Sci. USA 100, 13190–13195.
[4] Yang, S. et al. (2006) Synthesis, crystal structure, structure-activity relationships, and antiviral activity of a potent SARS coronavirus 3CL protease inhibitor. J. Med. Chem. 49, 4971–4980.
[5] Shao, Y.M. et al. (2007) Structure-based design and synthesis of highly potent SARS-CoV 3CL protease inhibitors. Chembiochem 8, 1654–1657.
[6] Hsu, J.T. et al. (2004) Evaluation of metal-conjugated compounds as inhibitors of 3CL protease of SARS-CoV. FEBS Lett. 574, 116–120.
[7] Someya, Y., Takeda, N. and Miyamura, T. (2005) Characterization of the norovirus 3C-like protease. Virus Res. 110, 91–97.
[8] Han, Y.S. et al. (2005) Papain-like protease 2 (PLP2) from severe acute respiratory syndrome coronavirus (SARS-CoV): expression, purification, characterization, and inhibition. Biochemistry 44, 10349–10359.
[9] Dhanak, D. et al. (2000) Metal mediated protease inhibition: design and synthesis of inhibitors of the human cytomegalovirus (hCMV) protease. Bioorg. Med. Chem. Lett. 10, 2279–2282.
[10] Tong, L. et al. (1996) A new serine-protease fold revealed by the crystal structure of human cytomegalovirus protease. Nature 383, 272–275.
[11] Yeung, K.S. et al. (2001) Structure-activity relationship studies of a bisbenzimidazole-based, Zn(2+)-dependent inhibitor of HCV NS3 serine protease. Bioorg. Med. Chem. Lett. 11, 2355–2359.
[12] Kuo, C.J. et al. (2004) Characterization of SARS main protease and inhibitor assay using a fluorogenic substrate. Biochem. Biophys. Res. Commun. 318, 862–867.
[13] Otwinowski, Z. and Minor, W. (1997) in: Processing of X-ray Diffraction Data Collected in Oscillation Mode (Sweet, R.M., Ed.), pp. 307–326, Academic, New York.
[14] Navaza, J. (1994) AMoRe: an automated package for molecular replacement. Acta Crystallogr. A 50, 157–163.
[15] Brünger, A.T. et al. (1998) Crystallography & NMR system: a new software suite for macromolecular structure determination. Acta Crystallogr. D 54, 905–921.
[16] McRee, D.E. (1999) XtalView/Xfit – a versatile program for manipulating atomic coordinates and electron density. J. Struct. Biol. 125, 156–165.
[17] Katz, B.A. et al. (1998) Design of potent selective zinc-mediated serine protease inhibitors. Nature 391, 608–612.
[18] Christianson, D.W. and Lipscomb, W.N. (1986) X-ray crystallographic investigation of substrate binding to carboxypeptidase A at subzero temperature. Proc. Natl. Acad. Sci. USA 83, 7568–7572.
[19] Brewer, G.J. et al. (2000) Treatment of Wilson's disease with zinc. XVII: treatment during pregnancy. Hepatology 31, 364–370.
[20] Sharquie, K.E. et al. (2006) Oral zinc sulfate in the treatment of Behcet's disease: a double blind cross-over study. J. Dermatol. 33, 541–546.
[21] Sakurai, H. and Adachi, Y. (2005) The pharmacology of the insulinomimetic effect of zinc complexes. Biometals 18, 319–323.
[22] Dougherty, W.G. and Semler, B.L. (1993) Expression of virus-encoded proteinases: functional and structural similarities with cellular enzymes. Microbiol. Rev. 57, 781–822.
[23] Sverdlov, E.D. et al. (1989) Insertion of short hepatitis virus A amino acid sequences into poliovirus antigenic determinants results in viable progeny. FEBS Lett. 257, 354–356.